

Gamma Mixture Classifier for Plaque Detection in Intravascular Ultrasonic Images

Gonzalo Vegas-Sánchez-Ferrero, *Member, IEEE*, José Seabra, *Member, IEEE*, Oriol Rodríguez-Leor, Angel Serrano-Vida, Santiago Aja-Fernández, César Palencia, Marcos Martín-Fernández, and Joao Sanches, *Senior Member, IEEE*

Abstract—Carotid and coronary vascular incidents are mostly caused by vulnerable plaques. Detection and characterization of vulnerable plaques are important for early disease diagnosis and treatment. For this purpose, the echomorphology and composition have been studied. Several distributions have been used to describe ultrasonic data depending on tissues, acquisition conditions, and equipment. Among them, the Rayleigh distribution is a one-parameter model used to describe the raw envelope RF ultrasound signal for its simplicity, whereas the Nakagami distribution (a generalization of the Rayleigh distribution) is the two-parameter model which is commonly accepted. However, it fails to describe B-mode images or Cartesian interpolated or subsampled RF images because linear filtering changes the statistics of the signal.

In this work, a gamma mixture model (GMM) is proposed to describe the subsampled/interpolated RF images and it is shown that the parameters and coefficients of the mixture are useful descriptors of speckle pattern for different types of plaque tissues. This new model outperforms recently proposed probabilistic and textural methods with respect to plaque description and characterization of echogenic contents.

Classification results provide an overall accuracy of 86.56% for four classes and 95.16% for three classes. These results evidence the classifier usefulness for plaque characterization. Additionally, the classifier provides probability maps according to each tissue type, which can be displayed for inspecting local tissue composition, or used for automatic filtering and segmentation.

I. INTRODUCTION

VULNERABLE plaque consists of a collection of blood cells and cholesterol in the wall artery which is prone to causing cardiovascular problems such as heart attack and brain stroke [1], [2]. Generally, these lesions feature a thin fibrous cap over a soft lipid pool. The presence of these structures in the arterial wall causes a high mechanical stress in the arterial wall and, eventually, leads to rup-

ture of the vulnerable plaque and clots. Stenosis is another problem derived from the presence of plaques.

Among the imaging techniques commonly used for detecting atherosclerotic plaques in the coronary arteries, invasive coronary angiography has been considered as the standard. However, most patients with acute coronary syndromes have minimal or mild coronary lumen obstruction detected by angiography and this modality has proved to have a limited ability to accurately measure the degree of stenosis and to characterize plaque morphology [2]. Given these limitations, the importance of detecting stenosis areas and the presence of different kinds of plaque becomes evident. Instead of angiography, intravascular ultrasonography (IVUS) has been demonstrated to provide clear visualization of arterial wall inner morphology and a convenient alternative method for assessing the severity of morphology lesions [2].

The technical procedure of acquiring IVUS data uses a catheter similar to the standard catheters employed in coronary angioplasty. The catheter is inserted inside the artery and moved until it reaches the artery segment to be studied. A rotating piezoelectric transducer transmits acoustic pulses and collects the A-lines that correspond to the reflected echoes along the depth, ρ , for each direction θ . The result is a polar representation of a 360° cross-sectional view. This image is interpolated and geometrically arranged to build the Cartesian image. In Fig. 1, an example of an IVUS image in polar and Cartesian coordinates is depicted.

The acoustic response of different kinds of plaque is qualitatively known: lipidic plaque presents low echolucent response; fibrous plaque presents intermediate level echogenicity; and calcified plaque is hyperechogenic and usually presents an acoustic shadow because of the series of echoes created by multiple reflections within a small but highly reflective tissue [2]–[5].

Although this qualitative characterization of the plaques offers an intuitive interpretation of IVUS images, an important effort has been made to understand the echomorphology and pathological evolution [6]. Quantitative characterization of plaques allows developing or refining methods for plaque detection, risk predictions, and potentially suggesting different therapies.

To obtain a quantitative characterization of the ultrasonic response of plaques, the physics of ultrasound imaging should be taken into account. Basically, the process of image formation in medical ultrasound begins with a pulse packet emission which travels along the beam vector

Manuscript received June 20, 2013; accepted September 23, 2013. The authors acknowledge Junta de Castilla y León for grants VA37A611-2 and VA0339A10-2; Ministerio de Ciencia e Innovación for grants CEN-20091044, TEC2010-17982, and MTM2007-63257; and the Instituto de Salud Carlos III for grant PI11/01492.

G. Vegas-Sánchez-Ferrero, S. Aja-Fernández, C. Palencia, and M. Martín-Fernández are with the Laboratorio de Procesado de Imagen, Universidad de Valladolid, Valladolid, Spain (e-mail: gvegsan@lpi.tel.uva.es).

J. Seabra and J. Sanches are with the Institute for Systems and Robotics, Department of Bioengineering (DBE), Instituto Superior Técnico/Technical University of Lisbon, Lisbon, Portugal.

O. Rodríguez-Leor is with the Hospital Universitario Germans Trias i Pujol, Badalona, Spain.

A. Serrano-Vida is with the Hospital General de Granollers, Granollers, Spain.

DOI <http://dx.doi.org/10.1109/TUFFC.2014.2878>

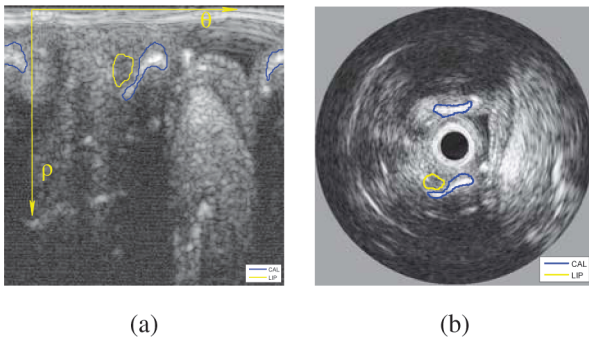



Fig. 1. Intravascular ultrasonography image in (a) polar coordinates and (b) Cartesian coordinates with the presence of lipidic (LIP) and calcified (CAL) plaques that were histologically identified. 

axis and changes shape according to characteristics of the media.

The traveling pulse is scattered by objects placed at different scattering depths, causing delays in the pulse. The backscattered (received) signal is corrupted by a characteristic granular pattern noise called speckle, which depends on the number of scatterers per resolution cell as well as their size [7], [8]. This type of multiplicative noise, in the sense that its variance depends on the underlying signal, is observed in other modalities using coherent radiation such as lasers [9] and synthetic-aperture radar (SAR) [10].

Speckle mainly depends on the microstructure of the tissues, and thus its statistics can be used as tissue histological descriptors [11]. These statistics strongly depend on the effective scatterer density; that is, on the effective number and intensity distribution of the scatterers in each resolution cell, their size, their shape, and their spatial organization, as well as the acquisition instrumentation and the tissue attenuation [12]–[14]. The resulting speckle noise can be grouped in the following main classes:

- Fully developed: an infinite effective number of scatterers per resolution cell and no deterministic component, modeled by the Rayleigh distribution in the case of one-parameter distribution [15]–[18].
- Possibly fully resolved: an infinite effective number of scatterers per resolution cell and possible existence of a deterministic component, modeled by Rice distribution [19]–[21].
- Possibly partially developed: an arbitrary effective number of scatterers per resolution cell and no deterministic component, modeled by K distribution [12], [22], [23].
- Possibly partially resolved: an arbitrary effective number of scatterers per resolution cell and possible existence of a deterministic component, modeled by homodyned K -distribution [24], [25].

Fully developed speckle is the most common model for speckle formation. It considers a tissue or region composed of a large number of scatterers acting as echo diffusers. These scatterers arise from inhomogeneity and structures

approximately equal to or smaller in size than the wavelength of the ultrasound, such as tissue parenchyma, where there are changes in acoustic impedance on a microscopic level within the tissue. Under this condition, pixel intensities in envelope data were usually modeled by Rayleigh probability density functions (PDFs) [7], [18], [26].

Note that the most general case of speckle is the possibly partially resolved case, which is modeled by a homodyned K -distribution. The K -distribution is a special case of the homodyned K -distribution with no deterministic component. The Rice distribution is the limiting case corresponding to an infinite effective density. The Rayleigh distribution is a special case of the Rice distribution with no deterministic component.

Other distributions have been proposed for the characterization of speckle. Probably the most noticeable distribution is the Nakagami distribution proposed in [27]. This distribution has two parameters and can be considered as a generalization of the Rayleigh distribution. In [13], a model based on Nakagami distributions is proposed for the characterization of backscattered echo. This model is motivated by the fact that the Nakagami distribution generalizes the Rayleigh distribution and also appears to be similar to Rician distribution, which is also a generalization of the Rayleigh distribution (see [13]). This is the reason that the Nakagami distribution is the commonly accepted distribution for speckle, and it is also considered as the two-parameter approximation of the true distribution for all the cases (without log-compression or application of filters) [13], [14], [28], [29].

The distribution of speckle depends not only on the tissues but on the acquisition process and the post-processing. The transducer center frequency also affects the distributions. Note that as the central frequency increases, the size of the range cell shrinks and, thus, the number of scatterers in the range cell decreases and one must expect non-Rayleigh statistics. This can be seen as an additional reason for the better fitting of other two-parameter distributions such as the gamma distribution. Additionally post-processing techniques such as log-compression and filtering also affect the probability distributions of speckle.

Plaque echomorphology is the contribution result of different tissue types (components). The lipidic plaque usually presents a fibrotic cap, which has different acoustic response and thus different distributions [2]. Additionally, accumulation of blood cells (macrophages) within plaques may change their probabilistic models. Hence, a mixture model becomes an opportune strategy for statistically describing the echomorphology of the plaque.

The Rayleigh mixture model (RMM) was first proposed in [8], [30] for plaque characterization and classification. In that work, an RMM was obtained by the expectation-maximization method [31], [32]. Three kinds of plaque were considered in that study: fibrotic, lipidic, and calcified. The RMM parameters were estimated for each kind of plaque and were used, in combination with other textural features, to provide a descriptor of plaque composition. On the other hand, a Nakagami mixture model

(NMM) was proposed in [28] for segmentation of arteries. This approach uses the Nakagami distribution as a generalization of Rayleigh distribution as a good candidate to characterize the speckle.

The Rayleigh distribution has been an accepted assumption for fully developed speckle [13], [26], [33], [34]. Its generalization by means of the Nakagami distribution has been used as an approximate general model for the echo envelope [13]. However, in the presence of downsampling with interpolation, the reported tests indicate that Rayleigh or Nakagami models do not fit the data as well as the gamma distribution.

In [33], many distributions were fitted to generic B-mode images having undergone log-compression and filtering. Results showed that speckle is better described by the gamma distribution, though no theoretical justifications were provided for this better fitting. Additionally, in [34], some distributions were also empirically tested for the envelope signal without further processing, showing a better fit for the gamma distribution.

In [7], the gamma distribution's performance was compared with other distributions when interpolated fully developed speckle was considered. Experimental tests have shown the superiority of the gamma distribution over the Rayleigh and Nakagami for describing ultrasound (US) data—85% of the fully developed speckle areas passed the χ^2 test when a gamma distribution was fitted, compared with 70% and less than 10% passed in the Nakagami and Rayleigh cases, respectively.

The interpolation operation performed in the A-lines of the raw RF signal to resample the data and equalize the resolution in both dimensions, angle and depth, seems to be the key element to explain why the gamma distribution describes the data better than the Rayleigh or Nakagami distributions. The interpolation process can be formulated as linear filter that linearly combines different pixels that are Rayleigh distributed. As shown in [7], a linear combination of Rayleigh random variables can be accurately fitted by gamma distributions.

Note that the interpolation process consists of a weighted sum of values that, in the case of Rayleigh distributed data, results in a different random variable. Hence, not only interpolation processes but every linear filter applied to Rayleigh distributed data are a weighted sum of Rayleigh random variables, which is better described by a gamma random variable than a Rayleigh.

In [35], the authors presented a bimodal gamma distribution with five parameters to model the statistics of the pixels in the gray-level (B-mode) images. The parameters of the distribution were evaluated for regions containing plaque using curve-fitting techniques. In that work, just two gamma distributions were used because of the limitations of curve-fitting techniques applied. The model showed good fitting properties for hard (calcified) plaque and soft plaque (lipids, cellular components, and loose connective tissue).

In [36], some mixtures of gamma distributions are also suggested, this time for wireless channels, where they

show a better fitting results than Rayleigh or Nakagami distributions.

A common stage of the acquisition process of US images is to downsample the acquired signal to provide an isotropic image resolution. This resampling stage usually involves an interpolation stage in which linear filtering is applied. In these conditions, the results obtained in [7] and [34] still hold and the Gamma distribution better describes US RF envelope downsampled data than the Rayleigh or Nakagami distributions.

The objective of this work is threefold: 1) propose a gamma mixture model (GMM) to describe the interpolated/resampled RF envelope US data; 2) based on the parameters and coefficients of this mixture, design and train a classifier to discriminate calcified, lipidic, fibrotic, and lumen regions within atherosclerotic plaques; and 3) provide probability maps which can be of help for physicians or for automatic postprocessing techniques such as filtering or segmenting methods.

GMM and a method based on RMM [30] are compared in terms of goodness of fit and classification accuracy. Comparison results showed that the GMM outperforms the RMM in terms of goodness of fit as well as accuracy. Besides the approaches by probabilistic speckle characterization, some methods have been proposed based on textural analysis. These methods usually consider autoregressive models, spectral features, or wavelet coefficients [30], [37]–[39]. The proposed classifier is also compared with a recently published method based on textural features [38]. Results showed that the proposed method outperforms both the textural-based and the RMM classifier in 5% and 22.7% of accuracy, respectively.

The rest of the paper is structured as follows: In Section II, we describe the data set, the acquisition protocols, and histological validation for plaques. In Section III, we test the capability of the most commonly used distributions for describing the probabilistic behavior of speckle (i.e., Rayleigh, Nakagami, gamma). In Section IV, the GMM is proposed. Section V is devoted to the GMM classifier, where the mixture of GMMs is proposed and derived. The experiments are presented in Section VI; first, the optimal number of components for each tissue class is analyzed; second, the proposed classification method is compared with those of [30] and [38]; third, the statistical significance of the classification results is tested by means of the Friedman test and Bonferroni–Dunn test; and fourth, probability maps are presented. Finally, we conclude in Section VII.

II. MATERIALS

Having a gold standard to test the performance of classifiers is of great importance; however, the only way to assess the nature of plaques and their location is by histological validation. In this work, the classification is tested with the gold standard obtained using the methodology recently presented in [38]. The IVUS data set consists of

9 post-mortem coronary arteries obtained from 9 different patients. All the patients died by sudden death of uncertain origin or accidental death, so there was no indication of cardiac problems. Note that the fact that the subjects did not have any symptoms of coronary disease does not necessarily mean that coronary atheromatosis is not present in the arteries [40]. The relatives of the deceased gave written informed consent to use their arteries. The samples of the coronary arteries were obtained in the University Hospital Germans Trias i Pujol (Badalona, Spain) with the approval of its ethical committee. The analysis of the post-mortem arteries was performed at the hemodynamic department of the same hospital, under the supervision of Dr. J. Mauri and Dr. O. Rodriguez-Leor.

From these arteries, 50 different images with the presence of plaques of different nature were selected. Then, the arteries are sectioned to characterize plaques by histological analysis. The histological analysis was performed in the General Hospital of Granollers (Granollers, Spain) by the pathologist Dr. A. Serrano-Vida.

The acquisition of the images was performed in the following way: The artery is separated from the heart, fixed in a mid-soft plane, and filled (using a catheter) with physiological saline solution at constant pressure [around 16 kPa (120 mmHg)], simulating blood pressure. References of distal, proximal, and left and right positions are marked. The probe is introduced through the catheter and RF data are acquired in correspondence with plaques.

Real-time RF data acquisition was performed with the Galaxy II IVUS imaging system (BostonScientific Corp., Natick, MA) using a catheter Atlantis SR Pro 40MHz (Boston Scientific Corp.). To collect and store the RF data, the imaging system has been connected to a workstation equipped with a 12-bit Acquiris acquisition card (Agilent Technologies Inc., Santa Clara, CA) with a sampling rate of 200 MHz.

The RF data for each frame is arranged in a matrix of $N \times M$ samples, where $M = 1024$ is the number of samples per A-line, and $N = 256$ is the number of positions assumed by the rotational ultrasound probe.

The histological validation of plaques comprises the following steps: vessels are cut in correspondence with previously marked positions and plaque composition is determined by histological analysis. A correspondence between

detected plaques by histology and respective IVUS image is established by means of reference positions set by an expert interventionist (Dr. O. Rodriguez-Leor) in cooperation with the pathologist (Dr. A. Serrano-Vida).

With the purpose of preserving a reliable correspondence between histological tissue and regions of the IVUS image, the medical team manually performs the plaque labeling task, discarding pairs of images in which a correspondence cannot be obtained.

Finally, the data set comprises 50 different images obtained from 9 different arteries (patients). All of them present a segmentation of the lumen (50 lumen regions, one per image); a set of 69 plaques was identified in the images and histologically characterized as the following types: 30 calcified, 14 lipidic, and 25 fibrotic. Table I shows the distribution of plaques among the patients (arteries) in the data set.

To provide comparable features between patients, we applied the following acquisition protocol: the IVUS images have been directly reconstructed from the raw RF signals rather than using the ones produced by the IVUS equipment. The image reconstruction algorithm used in this work is the one described in [38] and it is shown in Fig. 2. The process comprises the following stages:

- 1) Time-gain compensation, with $TGC(r) = 1 - e^{-\beta r}$ where $\beta = \log 10^{\alpha f/20}$, α is the attenuation coefficient for biological soft tissues ($\alpha \approx 0.8$ dB/MHz-cm for $f = 40$ MHz [38]), f is the central frequency of the transducer in megahertz and r is the radial distance from the catheter in centimeters.
- 2) Butterworth band-pass filter with cut-off frequencies $f_L = 20$ MHz and $f_H = 60$ MHz.
- 3) Envelope recovery with Hilbert transform.
- 4) Downsampling of the image to obtain isotropic resolution with linear filtering.
- 5) Log-compression.
- 6) Digital development process (DDP): a nonlinear adjustment of the gain and edge-emphasis process to enhance the tissue visualization.

After this reconstruction process, the IVUS displayed image can be easily obtained by interpolating polar coordinates into Cartesian coordinates, resulting in a non-

TABLE I. DATA SET OF 50 DIFFERENT IMAGES ACQUIRED FROM 9 DIFFERENT PATIENTS.

Patient (artery)	Number of images	Lipidic	Fibrotic	Calcified	Lumen
1	8	5	0	5	8
2	6	2	0	6	6
3	8	0	7	3	8
4	2	2	1	2	2
5	5	0	3	5	5
6	2	2	0	0	2
7	3	2	2	1	3
8	10	1	6	8	10
9	6	0	6	0	6
Total:	50	14	25	30	50

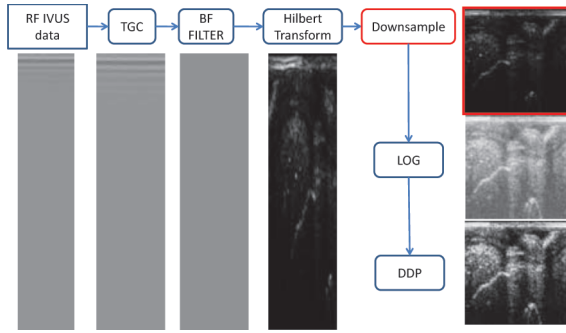



Fig. 2. Image reconstruction process. A time-gain compensation (TGC) operation is applied to the RF intravascular ultrasonography data acquired. The envelope is recovered by a Hilbert transform. A downsampling stage is applied to obtain isotropic resolution; all the analysis of this work is applied after this stage, in which the gamma assumption is applied. Log-compression and digital development process (DDP) stages are usually applied for visualization. 

compressed, 256×256 pixel image [cf. Fig. 1(a), where the polar coordinate image is shown and Fig. 1(b), where the interpolation into Cartesian coordinates is depicted].

The traditional displayed IVUS image is obtained from the polar representation (ρ, θ) by interpolating in a rectangular (Cartesian) grid, (i, j) . However, in this work, the image used for feature extraction and classification is the non-compressed polar image obtained after the downsampling step (cf. Fig. 2). This stage of the reconstruction process involves linear filtering (to downsample without aliasing) and, thus, Rayleigh or Nakagami models do not fit the data as well.

III. PROBABILISTIC MODEL FOR ENVELOPE DATA

In this section, the performance of Rayleigh, Nakagami, and gamma distributions are tested as candidates for describing the probabilistic behavior of speckle in the pre-processing stage of the envelope image formation process.

The performance test of both distributions is carried out after the downsampling stage (see Fig. 2), where the Nakagami distribution is commonly accepted. All envelope images of the data set (50 in total) were tested with two different measures: the Kullback–Leibler divergence and the uniform norm of the cumulative distribution function (CDF). The former is a non-symmetric measure of the difference between two probability distributions, defined as

$$\tilde{D}_{\text{KL}}(p_n, f_X) = \sum_{i=1}^N p_n(i) \log_2 \frac{p_n(i)}{f_X(i)}, \quad (1)$$

where p_n is the empirical PDF estimate and f_X is the theoretical distribution: Rayleigh, gamma, or Nakagami.

Note that the binary logarithm was chosen in this definition. We decided to use this base because the calculation of Kullback–Leibler divergence in other works such as [30] was provided in that base.

Instead of using the formulation of (1) we used the following symmetrized form:

$$D_{\text{KL}} = \frac{1}{2} (\tilde{D}_{\text{KL}}(p_n, f_X) + \tilde{D}_{\text{KL}}(f_X, p_n)). \quad (2)$$

The measure D_{KL} provides a symmetric way to measure the similarity between the PDFs. Because both the $\tilde{D}_{\text{KL}}(p_n, f_X)$ and $\tilde{D}_{\text{KL}}(f_X, p_n)$ are nonnegative, this measure is more restrictive than that of (1).

The empirical PDF was estimated by means of the histogram of the neighborhood of the pixel under study. The chosen neighborhood size is 11×11 ; the number of bins of the histogram is $n = 30$ equally spaced and smoothed with a Gaussian kernel (see [41] for more details). The smoothing process reduces the dependence of the PDF approximation on the number of bins used. Parameters of Rayleigh and gamma PDFs correspond to the maximum likelihood estimates of the data in the neighborhood of the pixel studied; parameters of the Nakagami distribution were calculated as in [42].

The uniform norm of the cumulative distribution function, also called Kolmogorov–Smirnov (KS) statistic, is defined as:

$$D_{\text{KS}} = \sup |\hat{F}(i) - F_X(i)|, \quad (3)$$

where \hat{F}_n is the empirical CDF of data and F_X is the CDF of the theoretical distributions.

This last metric was chosen because it does not depend on the number of bins used for the empirical PDF estimate and can be calculated with a small number of samples. Additionally, the Glivenko–Cantelli theorem states that, if the samples are drawn from distribution F_X , then D_{KS} almost surely converges to 0 [43].

As an example, in Fig. 3(a), a downsampled envelope image is depicted (it is log-compressed only to ease the visualization); Figs. 3(b)–3(d) show the Kullback–Leibler divergence, D_{KL} , computed for the Rayleigh, Nakagami, and gamma distributions, respectively. Figs. 3(e)–3(g) show the D_{KS} measure for Rayleigh, Nakagami, and gamma distributions respectively. This example shows a better performance of gamma distribution for both measures. The darker the image is, the better is the performance for both measures.

To provide a quantitative result of the performance of the gamma distribution in contrast to the Rayleigh and Nakagami distributions, a Welch t -test was performed for both measures, D_{KL} and D_{KS} , in the following way: for each of the images of the data set, both measures were calculated in each neighborhood (with size 11×11). For each image, the average value was calculated and, thus, the Welch t -test is performed with 50 samples. This test was chosen because no equal variance should be assumed. This test is performed considering pairs of distributions (gamma versus Rayleigh, gamma versus Nakagami, and Rayleigh versus Nakagami). The null hypothesis considers that both population means are the same. The boxplot of both measures is depicted in Figs. 3(h) and 3(i).

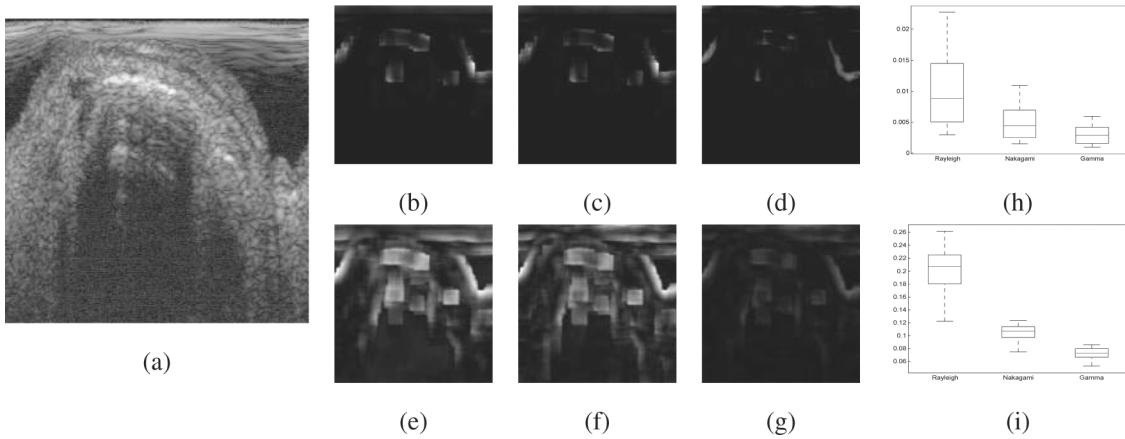


Fig. 3. (a) Log-compressed representation of the envelope. Kullback–Leibler divergence for (b) Rayleigh, (c) Nakagami, and (d) gamma distributions. Uniform norm of the cumulative distribution function for (e) Rayleigh, (f) Nakagami, and (g) gamma distributions. Boxplots for both measures D_{KL} and D_{KS} are represented in (h) and (i), respectively. Welch t -test results show that populations are statistically different and thus the gamma distribution fits better than Rayleigh or Nakagami distributions.

P -values of the Welch t -test for the case of Kullback–Leibler divergence and uniform norm of the CDF are shown in Table II. Note that all values are negligible and the null hypothesis must be rejected in all cases. Consequently, these three distributions fit in a different way, and the gamma distribution is the one with best fitting for both measures. Note that the Nakagami distribution was introduced as an approximate model for the echo envelope.

This result is a strong confirmation that gamma distribution better describes the probabilistic nature of speckle when internal preprocessing such as linear filtering (to avoid aliasing in the downsampling stage) are taking place, and confirms the result obtained in [7], where the better performance of the gamma was justified as the result of the linear filtering of fully formed speckle.

The gamma distribution also showed a better fit in [34], where the experiments were carried out directly from the envelope data after RF band-pass filtering. However, in our case, we are extending this result to the case of filtering after the envelope detection to rearrange and down-sample the data.

IV. GAMMA MIXTURE MODEL

In this section, the gamma mixture model is proposed and the method for the computation of its parameters and coefficients is described. The goal of using GMMs is that

TABLE II. P -VALUES FOR THE WELCH T -TEST FOR THE CASES OF D_{KL} AND D_{KS} .

	Rayleigh	Nakagami	Gamma
Rayleigh	—	$7.54 \cdot 10^{-35}$	$7.9 \cdot 10^{-38}$
Nakagami	$7.6 \cdot 10^{-11}$	—	$3.67 \cdot 10^{-46}$
Gamma	$3.47 \cdot 10^{-17}$	$1.69 \cdot 10^{-16}$	—

Values below the diagonal: Kullback–Liebler divergence; values above the diagonal: Kolmogorov–Smirnov statistic.

the echomorphology may result from the contribution of different echogenic components of the plaque that follow different distributions. Under the assumption of gamma-distributed speckle, the GMM arises in a natural way.

Let $\mathbf{X} = \{x_i\}$, $1 \leq i \leq N$ be a set of samples (pixel intensities) of a given region of the ultrasound image. These samples can be considered as independent and identically distributed (IID) random variables (RVs). This assumption is taken because the downsampling stage reduces the possible correlation between neighboring pixels. The GMM considers that these variables result from the contributions of J distributions: ¹

$$p(x_i|\Theta) = \sum_{j=1}^J \pi_j f_X(x_i|\Theta_j), \quad (4)$$

where Θ is a vector of the parameters of the GMM ($\pi_1, \dots, \pi_J, \Theta_1, \dots, \Theta_J$) and Θ_j are the parameters of the PDF (in our case the parameters of a Gamma distribution are represented as α_j and β_j). The gamma PDF is defined as

$$f_X(x|\alpha, \beta) = \frac{x^{\alpha-1}}{\beta^\alpha \Gamma(\alpha)} e^{-x/\beta}, \quad x \geq 0 \text{ and } \alpha, \beta > 0, \quad (5)$$

where $\Gamma(x)$ is the Euler gamma function defined as $\Gamma(x) = \int_0^\infty t^{x-1} e^{-t} dt$, for $x > 0$. The condition $\sum_{j=1}^J \pi_j = 1$ must hold to guarantee that $p(x_i|\Phi)$ is a well-defined probabilistic distribution.

The joint distribution of IID samples is given by

$$p(\mathbf{X}|\Theta) = \prod_{i=1}^N p(x_i|\Theta). \quad (6)$$

The expectation-maximization method is applied here to maximize the log-likelihood function when some hidden

¹The notation used, from here forth, refers to random variables using capital letters and samples of random variables using lower case letters. The expectation operator is denoted $E\{\cdot\}$.

discrete RVs, $\mathbf{Z} = \{Z_j\}$, are introduced to the model. These RVs take values in $\{1, \dots, J\}$; their meaning is that the sample x_i belongs to the distribution class j when $Z_i = j$.

Now, let $\Theta^{(n)}$ be an estimate of the parameters of the mixture in the n th iteration; the expectation step is performed by calculating the expected value of the log-likelihood $\mathcal{L}(\Theta|\mathbf{X}, \mathbf{Z})$:

$$\mathcal{Q}(\Theta|\Theta^{(n)}, \mathbf{X}) = E_{\mathbf{Z}|\Theta^{(n)}, \mathbf{X}}\{\mathcal{L}(\Theta|\mathbf{X}, \mathbf{Z})\}. \quad (7)$$

In the maximization step, the new estimate $\Theta^{(n+1)}$ is obtained by maximizing the expectation of the likelihood function $\mathcal{Q}(\Theta|\Theta^{(n)}, \mathbf{X})$. These steps are iterated until a stop criterion such as $\|\Theta^{(n+1)} - \Theta^{(n)}\| < \text{TOL}$ for some pre-established threshold (TOL) is reached.

The application of the EM algorithm for general distributions is not new; see, for example, [32] and [44]. In the case of a GMM, it was first derived by Webb in [45]; other similar derivations were obtained in [28] and [42]. For the sake of completeness and to introduce the notation used to derive the classifier, the EM algorithm is explained in [28] and [45], which results in the following equality for the weights:

$$\hat{\pi}_j = \frac{1}{N} \sum_{i=1}^N \gamma_{i,j} = \frac{1}{N} \sum_{i=1}^N p(Z_i = j | x_i, \Theta^{(n)}). \quad (8)$$

where $\gamma_{i,j} = p(Z_i = j | x_i, \Theta^{(n)})$ to make notation simpler, and it can be derived by the Bayes theorem as

$$\gamma_{i,j} = p(Z_i = j | x_i, \Theta^{(n)}) = \frac{p(x_i | \Theta_j^{(n)}) p(Z_i = j | \Theta^{(n)})}{p(x_i | \Theta^{(n)})}, \quad (9)$$

where $p(Z_i = j | \Theta^{(n)}) = \pi_j^{(n)}$.

The estimates of the gamma distribution parameters result in the following equalities (see [42] and [45]):

$$\log(\hat{\alpha}_j) - \psi(\hat{\alpha}_j) = \log\left(\frac{\sum_{i=1}^N \gamma_{i,j} x_i}{\sum_{i=1}^N \gamma_{i,j}}\right) - \frac{\sum_{i=1}^N \gamma_{i,j} \log x_i}{\sum_{i=1}^N \gamma_{i,j}} \quad (10)$$

$$\hat{\beta}_j = \frac{1}{\hat{\alpha}_j} \frac{\sum_{i=1}^N \gamma_{i,j} x_i}{\sum_{i=1}^N \gamma_{i,j}}, \quad (11)$$

where $\psi(x)$ is the Digamma function, defined as $\psi(x) = \Gamma'(x) / \Gamma(x)$.

Note that this is the case of uniform prior weights proposed in [45], which is a special case of the Dirichlet prior weights proposed in [42].

The method is applied in the following way:

- 1) A first estimate of the hidden variables is obtained by means of any clustering method (k -means for example). For each cluster $j = \{1, \dots, J\}$, the parameters of the distribution $\Theta_j^{(0)}$ can be calculated by means of the moments method or maximum likelihood methods. Weights, $\hat{\pi}_j^{(0)}$, can be calculated ei-

ther as $1/J$ or as the number of elements of each cluster divided by the total number of elements. Set $n = 0$.

- 2) Expectation step. $\gamma_{i,j}$ is calculated from (9).
- 3) Maximization step. The estimate for $\hat{\alpha}_j$ is calculated from (10) and $\hat{\beta}_j$ is calculated from (11). $\hat{\pi}_j$ is calculated from (8).
- 4) $n = n + 1$.
- 5) Go to step 2 until $\|\Theta^{(n)} - \Theta^{(n-1)}\| < \text{TOL}$ is satisfied.

As an example, in Fig. 4, the GMM is used to fit different tissue types and compared with the output of the NMM proposed in [42] and the RMM proposed in [8]. Specifically, three mixture components were used in the fitting process for GMM, NMM, and RMM. At first sight, the performance of the gamma mixture is better. Quantitative results calculated with D_{KL} and D_{KS} for the whole data set are provided in Table III. In this case, numerical results show that plaques, which can be composed of different echolucent sources or echogenic structures such as fibrous caps, are properly fitted with a gamma mixture model and, potentially, the parameters of the mixture model could be a good descriptor of the tissue class under the operations of downsampling and interpolation. Nevertheless, an extended study of the behavior of the GMM, NMM, and RMM is presented in Section VI.

V. GMM CLASSIFIER

In this section, a classifier based on GMMs priors is derived. This classifier is inspired by the work of [10], where a Bayesian GMM approach is proposed. There are some important differences between that method and the one presented here. The first is that the method in [10] adopted a Bayesian approach for deriving the model. This methodology considers the parameters of the GMMs as random variables, and thus needs the definition of some prior distributions to characterize them. These distributions require their parameters to be manually initialized, which clearly affects, and may bias, the mixture model.

Instead of considering prior distributions which can be inaccurate and may bias the results of the model, we apply an expectation-maximization approach without prior on the parameters. The initial values of the GMM parameters are obtained from the training set according to each tissue class. The final labeling of the GMMs is then obtained according to the closest initial GMMs (with respect to the D_{KS}) for each tissue class and the probability of belonging to each tissue class is obtained by the Bayes theorem.

A. Formulation

We state the problem as a mixture model of GMMs in the following way: Let $\mathbf{X} = \{x_i\}$, $1 \leq i \leq N$ be a set of samples (pixel intensities) of a given region of the ultra-

TABLE III. FITTING OF DIFFERENT TYPES OF TISSUE USING GAMMA MIXTURE MODEL (GMM), NAKAGAMI MIXTURE MODEL (NMM), AND RAYLEIGH MIXTURE MODEL (RMM).

Tissue	D_{KL}			D_{KS}		
	GMM	NMM	RMM	GMM	NMM	RMM
Calcified	$4.37 \cdot 10^{-5}$	$1.06 \cdot 10^{-4}$	$2.65 \cdot 10^{-4}$	0.0080	0.0180	0.0359
Lipidic	$3.29 \cdot 10^{-3}$	$5.03 \cdot 10^{-3}$	$5.78 \cdot 10^{-3}$	0.0054	0.0114	0.0161
Fibrotic	$3.97 \cdot 10^{-3}$	$4.57 \cdot 10^{-3}$	$4.91 \cdot 10^{-3}$	0.0038	0.0078	0.0117
Lumen	$1.13 \cdot 10^{-2}$	$2.41 \cdot 10^{-2}$	$4.85 \cdot 10^{-2}$	0.0167	0.0341	0.0894

Bold values show the best fitting for each tissue class.

sound image. These samples are IID RVs. The GMM considers that these variables result from the contributions of J tissue classes and each PDF comprises R_j components for each $j \in \{1, 2, \dots, J\}$. This mixture model takes into account the presence of different echolucent responses of plaques:

$$p(x_i|\Theta) = \sum_{j=1}^J \nu_j \sum_{r=1}^{R_j} \pi_{j,r} f_X(x_i|\Theta_{j,r}), \quad (12)$$

where Θ is a vector consisting of all the GMM parameters, i.e., ν_j , $\pi_{j,r}$, and $\Theta_{j,r} = (\alpha_{j,r}, \beta_{j,r})$.

In (12), two conditions must be imposed to the component weights to assure that (12) is well defined as a true PDF:

$$\sum_{j=1}^J \nu_j = 1 \text{ and } \sum_{r=1}^{R_j} \pi_{j,r} = 1, \text{ for each } j = \{1, \dots, J\}. \quad (13)$$

Now, the joint distribution, under the assumption of IID RVs is the product over all the samples, as in (6).

To apply the expectation-maximization method, two hidden discrete RVs vectors are introduced, $\mathbf{Z} = \{Z_i\}$ and $\mathbf{W} = \{W_{i,j}\}$. The former, \mathbf{Z} , takes values onto the set of all possible tissue classes, i.e., $\{1, \dots, J\}$ and $Z_i = j$ means that sample x_i belongs to the tissue class j . The latter, $W_{i,j}$, takes values over $\{1, \dots, R_j\}$ and the meaning of $W_{i,j} = r$ is that sample x_i belongs to the r component of the tissue class j .

Both RVs are defined in such a way that there is an implicit relationship which makes sense from the point of view of conditional probability. For instance, $p(Z_i = j|\Theta)$

is the probability of belonging to tissue class j when the parameters of the mixtures are known and, in the mixture model of (12), can be identified as ν_j ; $p(W_{i,j} = r|Z_i = j, \Theta)$ is identified as $\pi_{j,r}$. The hierarchical relationship between Z_i and $W_{i,j}$ is shown in Fig. 5, where tissue classes are denoted as \mathcal{C}_j and each component of each tissue class is $\mathcal{B}_{j,r}$. Note that this relationship allows consideration of the sample x_i as a contribution of each component within each tissue class, which is a desired property to reflect the mixed composition of plaques. A detailed explanation on the EM method is presented in Appendix A.

Supposing the previous estimate for the parameters of the mixture model $[\Theta^{(v)}]$ is known, the log-likelihood function with both hidden variables is the following (see Appendix A):

$$\begin{aligned} \mathcal{L}(\Theta|\mathbf{X}, \mathbf{Z}, \mathbf{W}) &= \sum_{i=1}^N \log f_X(x_i|\Theta_{z_i, w_{i,z_i}}) \\ &+ \sum_{i=1}^N \log p(w_{i,z_i}|\Theta) p(z_i|\Theta). \end{aligned} \quad (14)$$

In the expectation step, the expectation is calculated over \mathbf{Z} and \mathbf{W} for known data \mathbf{x} and a previous estimate $\Theta^{(n)}$:

$$\begin{aligned} \mathcal{Q}(\Theta|\Theta^{(n)}, \mathbf{X}) &= E_{\mathbf{Z}, \mathbf{W}|\Theta^{(n)}, \mathbf{X}} \{ \mathcal{L}(\Theta|\mathbf{X}, \mathbf{Z}, \mathbf{W}) \} = \\ &\sum_{i=1}^N \sum_{j=1}^J \sum_{r=1}^{R_j} \gamma_{i,j,r} (\log f_X(x_i|\alpha_{j,r}, \beta_{j,r}) + \log(\nu_j \pi_{j,r})), \end{aligned} \quad (15)$$

where $\gamma_{i,j,r} = p(Z_i = j, W_{i,j} = r|x_i, \Theta^{(n)})$, which can be easily calculated by means of the Bayes theorem:

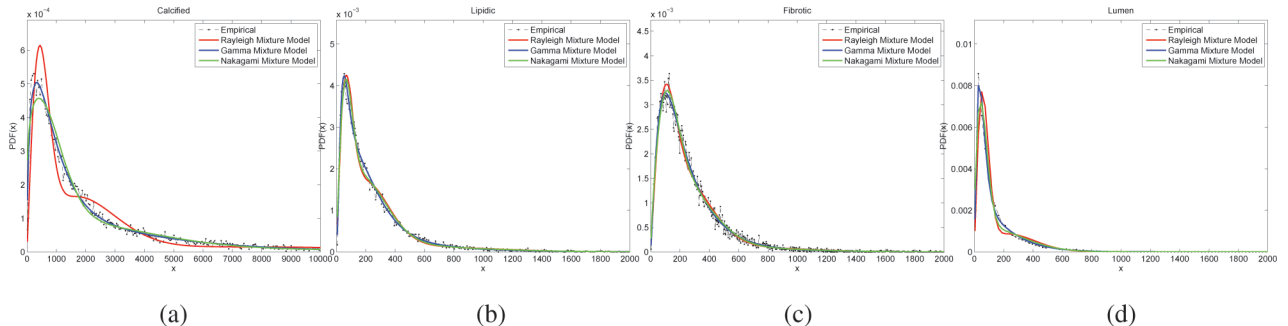


Fig. 4. Gamma, Nakagami, and Rayleigh mixture model fittings for (a) calcified, (b) lipidic, (c) fibrotic, and (d) lumen tissue. In all methods, the tolerance was fixed to $\|\Theta^{(n+1)} - \Theta^{(n)}\| < 10^{-4}$ with a maximum number of iterations of 1000 and three components in each mixture.

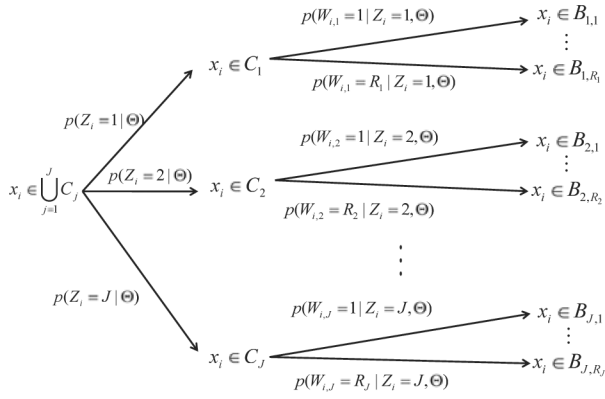


Fig. 5. Conditional probability scheme. Each sample x_i may belong to tissue class C_j with probability $p(Z_i = j | \Theta)$, and to the component $B_{j,r}$ with probability $p(W_{i,j} = r | Z_i = j, \Theta)p(Z_i = j, \Theta)$.

$$\gamma_{i,j,r} = \frac{f_X(x_i | \Theta_{j,r}^{(n)}) \nu_j^{(n)} \pi_{j,r}^{(n)}}{\sum_{k=1}^J \sum_{s=1}^{R_j} f_X(x_i | \Theta_{k,s}^{(n)}) \nu_k^{(n)} \pi_{k,s}^{(n)}}. \quad (16)$$

The updated weights can be calculated by the following equations:

$$\hat{\nu}_j = \frac{1}{N} \sum_{i=1}^N \sum_{r=1}^{R_j} \gamma_{i,j,r}, \quad \hat{\pi}_{j,r} = \frac{\sum_{i=1}^N \gamma_{i,j,r}}{\sum_{i=1}^N \sum_{s=1}^{R_j} \gamma_{i,j,s}}. \quad (17)$$

The updated parameters of the gamma mixtures can be calculated with the following equations:

$$\log(\hat{\alpha}_{j,r}) - \psi(\hat{\alpha}_{j,r}) = \log\left(\frac{\sum_{i=1}^N \gamma_{i,j,r} x_i}{\sum_{i=1}^N \gamma_{i,j,r}}\right) - \frac{\sum_{i=1}^N \gamma_{i,j,r} \log(x_i)}{\sum_{i=1}^N \gamma_{i,j,r}} \quad (18)$$

$$\hat{\beta}_{j,r} = \frac{1}{\hat{\alpha}_{j,r}} \frac{\sum_{i=1}^N \gamma_{i,j,r} x_i}{\sum_{i=1}^N \gamma_{i,j,r}}. \quad (19)$$

B. Training and Classifying

The training process is performed by estimating the prior parameters, $\Theta_{j,r}^{(0)}$ for the training set by fitting the GMMs explained in Section IV for each tissue class. Then, the mixtures of GMMs are fitted to the test set, $\mathbf{y} = \{y_i\}$ by the method explained in Section V-A in the following way:

- 1) Set $\Theta_{j,r}^{(0)}$, the prior parameters obtained by fitting the GMMs for the training set and for each tissue class. Initial weights are calculated as $\hat{\pi}_{j,r}^{(0)} = 1/R_j$ and $\hat{\nu}_j^{(0)} = 1/J$. Set $n = 0$.
- 2) Expectation step. $\gamma_{i,j,r}$ is calculated from (16).
- 3) Maximization step. $\hat{\beta}_{j,r}$ and $\hat{\alpha}_{j,r}$ are calculated from (19) and (18). $\hat{\nu}_j$ and $\hat{\pi}_{j,r}$ are calculated from (17).
- 4) $n = n + 1$.
- 5) Go to step 2 until $\|\Theta^{(n)} - \Theta^{(n-1)}\| < \text{TOL}$ is satisfied.

The GMM fitting can have more than one solution [46]. Actually, the parameters of the GMMs can be interchanged without affecting the fit with the data. To circumvent this problem, using D_{KS} , we compare the final distributions with the initial ones for each tissue class. Finally, the labels are assigned by considering the lower D_{KS} between the final distributions and the initial ones.

The posterior probability of belonging to each tissue class is then obtained by simply calculating the probability of $Z_i = j$ in the test set:

$$p(\mathbf{Z} = j | \Theta, \mathbf{y}) = \prod_{i=1}^N \frac{\sum_{r=1}^{R_j} \pi_{j,r} f_X(y_i | \Theta_{j,r}) \nu_j}{\sum_{k=1}^J \sum_{r=1}^{R_k} \pi_{k,r} f_X(y_i | \Theta_{k,r}) \nu_k}. \quad (20)$$

Finally, the selected class is that one with the highest posterior probability.

VI. EXPERIMENTAL RESULTS

In this section, two experiments are described. The first is related to the selection of the number of elements of the GMM which better fits to each tissue class. This experiment is also performed with RMM and NMM to see which of the gamma, Nakagami, or Rayleigh distributions better fits the ultrasound data under the operations of downsampling with interpolation.

The second experiment has the goal of classifying plaques into four tissue classes: calcified, lipidic, fibrotic, and lumen.

At the end of these tests, some examples of probability maps for each tissue class are shown. We believe that these maps provide useful information for manual analysis of plaque composition and we foresee its usage as a pre-processing step for automatic segmentation.

A. Optimal Number of Components for Each Class

Here, the GMM, NMM, and RMM have been applied to every presegmented plaque using an increasing number of components. We have used D_{KL} and D_{KS} to investigate the performance of GMM, NMM, and RMM with respect to the number of components for each class. The results are shown in Table IV.

Note that results of both measures evidence a better fit for the GMM for every tissue class. In all cases (GMM, RMM, and NMM) the performance is better as the number of components increases, but the GMM approach still remains as a better approach in nearly all of the cases.

These results can be used to select the number of components of the mixture models. Note that as the number of components increases, the measure decreases with a slower rate. In Fig. 6, the rate of decrease of both measures for GMM, RMM, and NMM are shown for each tissue class. This rate is calculated as $f_{\text{rate}}(n) = D(n-1) - D(n)$, where $D(n)$ is D_{KL} or D_{KS} measures and n is the number of components of the mixture model. This crite-

TABLE IV. GAMMA MIXTURE MODEL (GMM), NAKAGAMI MIXTURE MODEL (NMM), AND RAYLEIGH MIXTURE MODEL (RMM) FITTING FOR DIFFERENT KINDS OF TISSUE.

Tissue	D_{KL}			D_{KS}		
	GMM	NMM	RMM	GMM	NMM	RMM
2 components						
Calcified	$6.22 \cdot 10^{-5}$	$2.26 \cdot 10^{-4}$	$9.23 \cdot 10^{-4}$	0.0126	0.0331	0.1087
Lipidic	$6.32 \cdot 10^{-3}$	$1.26 \cdot 10^{-2}$	$3.36 \cdot 10^{-2}$	0.0198	0.0410	0.1059
Fibrotic	$4.26 \cdot 10^{-3}$	$7.58 \cdot 10^{-3}$	$1.21 \cdot 10^{-2}$	0.0085	0.0257	0.0445
Lumen	$1.73 \cdot 10^{-2}$	$5.71 \cdot 10^{-2}$	$3.94 \cdot 10^{-1}$	0.0277	0.0768	0.4110
3 components						
Calcified	$4.37 \cdot 10^{-5}$	$1.06 \cdot 10^{-4}$	$2.65 \cdot 10^{-4}$	0.0080	0.0180	0.0359
Lipidic	$3.29 \cdot 10^{-3}$	$5.03 \cdot 10^{-3}$	$5.78 \cdot 10^{-3}$	0.0054	0.0114	0.0161
Fibrotic	$3.97 \cdot 10^{-3}$	$4.57 \cdot 10^{-3}$	$4.91 \cdot 10^{-3}$	0.0038	0.0078	0.0117
Lumen	$1.13 \cdot 10^{-2}$	$2.41 \cdot 10^{-2}$	$4.85 \cdot 10^{-2}$	0.0167	0.0341	0.0894
4 components						
Calcified	$4.24 \cdot 10^{-5}$	$4.46 \cdot 10^{-5}$	$9.89 \cdot 10^{-5}$	0.0079	0.0072	0.0141
Lipidic	$3.29 \cdot 10^{-3}$	$3.98 \cdot 10^{-3}$	$4.26 \cdot 10^{-3}$	0.0055	0.0076	0.0083
Fibrotic	$3.96 \cdot 10^{-3}$	$4.23 \cdot 10^{-3}$	$4.07 \cdot 10^{-3}$	0.0032	0.0062	0.0036
Lumen	$6.44 \cdot 10^{-3}$	$2.39 \cdot 10^{-2}$	$1.18 \cdot 10^{-2}$	0.0043	0.0339	0.0126
5 components						
Calcified	$3.08 \cdot 10^{-5}$	$4.36 \cdot 10^{-5}$	$9.89 \cdot 10^{-5}$	0.0042	0.0071	0.0141
Lipidic	$3.09 \cdot 10^{-3}$	$3.79 \cdot 10^{-3}$	$3.88 \cdot 10^{-3}$	0.0044	0.0070	0.0060
Fibrotic	$3.95 \cdot 10^{-3}$	$4.23 \cdot 10^{-3}$	$4.03 \cdot 10^{-3}$	0.0029	0.0062	0.0033
Lumen	$6.44 \cdot 10^{-3}$	$9.76 \cdot 10^{-3}$	$1.12 \cdot 10^{-2}$	0.0044	0.0117	0.0110
6 components						
Calcified	$3.07 \cdot 10^{-5}$	$4.25 \cdot 10^{-5}$	$4.77 \cdot 10^{-5}$	0.0041	0.0068	0.0036
Lipidic	$2.94 \cdot 10^{-3}$	$3.39 \cdot 10^{-3}$	$3.68 \cdot 10^{-3}$	0.0029	0.0057	0.0065
Fibrotic	$3.95 \cdot 10^{-3}$	$4.13 \cdot 10^{-3}$	$4.01 \cdot 10^{-3}$	0.0031	0.0054	0.0031
Lumen	$6.18 \cdot 10^{-3}$	$9.39 \cdot 10^{-3}$	$8.90 \cdot 10^{-3}$	0.0031	0.0110	0.0118
7 components						
Calcified	$3.08 \cdot 10^{-5}$	$4.30 \cdot 10^{-5}$	$4.77 \cdot 10^{-5}$	0.0041	0.0069	0.0036
Lipidic	$2.93 \cdot 10^{-3}$	$3.40 \cdot 10^{-3}$	$3.66 \cdot 10^{-3}$	0.0026	0.0059	0.0066
Fibrotic	$3.94 \cdot 10^{-3}$	$4.07 \cdot 10^{-3}$	$4.00 \cdot 10^{-3}$	0.0024	0.0047	0.0029
Lumen	$6.18 \cdot 10^{-3}$	$6.83 \cdot 10^{-3}$	$8.90 \cdot 10^{-3}$	0.0031	0.0052	0.0118

Bold values show the best fitting for each tissue class.

tion takes into account the lowest number of components per tissue class for which the goodness of fit does not significantly improve when another component is added to the mixture model. Note that the global maximum is obtained for $n = 3$. From that value, the differences are lower than that observed for 3 components.

Other selection criteria could be applied. We also applied the Bayesian information criterion (BIC) [47] to determine the preferred number of components for each tissue class. This criterion provides the preferred model for a finite set of models, which is the case. It is based on calculating the log-likelihood and penalizing distributions with a higher number of free parameters to avoid over-fitting.

The number of free parameters used for the RMM is $2 \times$ the number of components $- 1$, because each Rayleigh has one parameter and the number of free weights is the number of components $- 1$ because the sum of weights must be 1. In the case of GMM and NMM, it is $3 \times$ the number of components $- 1$, for the same reason (both gamma and Nakagami have 2 parameters).

The BIC criterion is obtained by means of the following formula:

$$\text{BIC} = -2 \log(L) + k \log(n), \quad (21)$$

where L is likelihood function for the estimated model, k is the number of free parameters of the model, and n is the number of samples.

The obtained preferences for each tissue class are shown in Table V as well as the number of free parameters and the D_{KL} . These results show the goodness of fit of the mixture models, penalizing loss of degree of freedom by having more parameters in the fitted model. In all cases, the D_{KL} is lower than that obtained by NMM and RMM. The gamma distribution provides the least number of components for describing all tissue classes. It also provides the least number of free parameters with the exception of calcified and fibrotic tissues. In the case of calcified tissue, one can choose a GMM of 3 components (8 free parameters) which provides a $D_{KL} = 4.37 \cdot 10^{-5}$ (see Table IV). This value is still lower than the one obtained for the RMM and almost equal to NMM and allows us to simplify the mixture model to prevent over-fitting in the training step. If we decrease the number of components (and free parameters) of NMM and RMM, the D_{KL} considerably increases (see Table IV) and the results are worse than the ones obtained for the GMM.

For the case of fibrotic tissue, the RMM requires fewer free parameters to be calculated. However, the lower num-

TABLE V. PREFERRED NUMBER OF COMPONENTS AND FREE PARAMETERS FOR EACH TISSUE CLASS CALCULATED BY USING THE BAYESIAN INFORMATION CRITERION.

Tissue	GMM	NMM	RMM
Calcified			
Components	5	5	6
Free parameters	14	14	11
D_{KL}	$3.08 \cdot 10^{-5}$	$4.36 \cdot 10^{-5}$	$4.77 \cdot 10^{-5}$
Lipidic			
Components	3	6	6
Free parameters	8	17	11
D_{KL}	$3.29 \cdot 10^{-3}$	$3.39 \cdot 10^{-3}$	$3.68 \cdot 10^{-3}$
Fibrotic			
Components	3	4	4
Free parameters	8	11	7
D_{KL}	$3.97 \cdot 10^{-3}$	$4.23 \cdot 10^{-3}$	$4.07 \cdot 10^{-3}$
Lumen			
Components	4	6	7
Free parameters	11	17	13
D_{KL}	$6.44 \cdot 10^{-3}$	$9.39 \cdot 10^{-3}$	$8.9 \cdot 10^{-3}$

Bold values show the best fitting for each tissue class.

ber of components of the GMM avoids the effect of overfitting during the classification step, as we show in a classification experiment presented in a later section (Table VI).

The lower preferred number of components in the GMM and NMM models compared with the RMM show better fitting to the data. However, considering the pictures shown in Fig. 6, the incremental gain of the fitting measures is negligible for so many components and the BIC criterion can be relaxed to 3 components. Nevertheless, in the next section we classify with an increasing number of components and the best cases of each mixture model are considered for comparisons.

B. Plaque Classification According to Tissue Type

In this experiment, the classifier explained in Section VI is applied for the whole data set with the leave-one-patient-out (LOPO) cross-validation technique. This method performs the classification by excluding all the images that come from the same patient of the plaque which is being classified. This is a technique for assessing the statistical independence of classification and, thus, avoids the problem of correlation between images from the same patient in the validation stage.

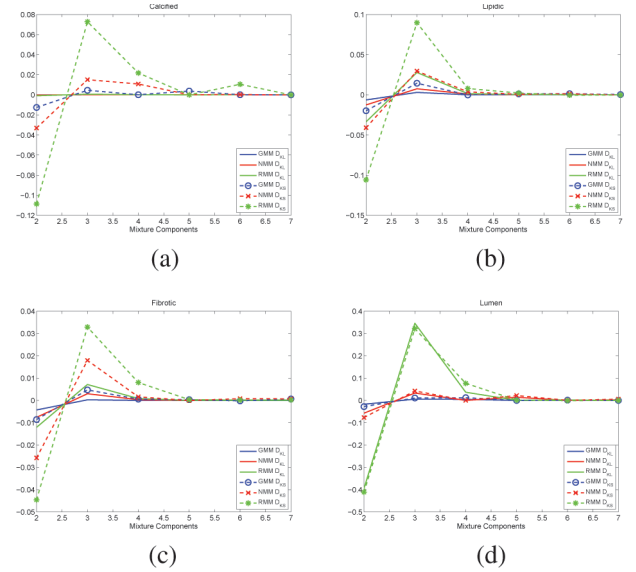


Fig. 6. Difference rate of D_{KL} and D_{KS} for gamma mixture model (GMM), Rayleigh mixture model (RMM), and Nakagami mixture model (NMM) for (a) calcified, (b) lipidic, (c) fibrotic, and (d) lumen tissue.

The classification is performed by partitioning the data into two complementary subsets. One of the sets contains all the images from the same patient and it is used for validation (validation set), whereas its complementary subset (the other patients) is considered as the analysis set and is used for the training step (training set).

The training set is used to obtain the initial values of the GMM parameters according to each tissue class. Then, the expectation-maximization method is applied to the image under study which belongs to the validation set and the GMMs fit to the whole image. The resulting GMMs are used to obtain the probability of belonging to each tissue class, which is obtained by the Bayes theorem.

Table VI shows the classification performance for an increasing number of components and free parameters for each mixture model in terms of global accuracy, $A = (TP + TN)/(TP + TN + FP + FN)$, where FN and FP stand for false negatives and false positives, respectively; TN and TP stand for true negatives and true positives. Note that the highest value of accuracy is reached for three components for both the GMM and the NMM. This confirms the relation between the classification and the fitting measures and shows that the GMMs and NMMs are good

TABLE VI. CLASSIFICATION PERFORMANCE FOR AN INCREASING NUMBER OF COMPONENTS AND FREE PARAMETERS PER TISSUE OF GAMMA MIXTURE MODEL (GMM), NAKAGAMI MIXTURE MODEL (NMM), AND RAYLEIGH MIXTURE MODEL (RMM).

	Components (Free parameters)					
GMM	2 (5)	3 (8)	4 (11)	5 (14)	6 (17)	7 (20)
Performance	73.95%	86.56%	82.35%	81.51%	73.11%	75.63%
NMM	2 (5)	3 (8)	4 (11)	5 (14)	6 (17)	7 (20)
Performance	77.31%	83.19%	79.83%	78.15%	78.99%	76.13%
RMM	2 (3)	3 (5)	4 (7)	5 (9)	6 (11)	7 (13)
Performance	31.93%	63.86%	68.07%	71.42%	71.27%	70.79%

Bold values show the best classification performance.

TABLE VII. PERFORMANCE OF TISSUE CLASSIFICATION.

	RMM classifier	NMM classifier	Textural classifier	GMM classifier
<i>A</i>	71.42	83.19	81.51	86.56
<i>S</i> _{Cal}	96.67	96.67	96.67	96.67
<i>S</i> _{Lip}	50.00	35.71	57.14	42.86
<i>S</i> _{Fib}	20.00	72.00	48.00	76.00
<i>S</i> _{Lum}	88.00	94.00	96.00	98.00
<i>K</i> _{Cal}	93.33	94.59	98.55	96.10
<i>K</i> _{Lip}	81.25	93.07	87.25	95.10
<i>K</i> _{Fib}	88.89	94.19	93.41	93.33
<i>K</i> _{Lum}	95.35	92.86	96.08	96.43
<i>P</i> _{Cal}	87.88	87.88	96.67	90.63
<i>P</i> _{Lip}	28.00	41.67	38.10	54.55
<i>P</i> _{Fib}	33.33	78.26	66.67	76.00
<i>P</i> _{Lum}	95.65	92.16	96.00	96.08

RMM = Rayleigh mixture model; NMM = Nakagami mixture model; GMM = gamma mixture model; A = accuracy; S = sensitivity; K = specificity; P = precision.

Bold values show the best classification performance.

descriptors of the behavior of the probabilistic nature of speckle in each tissue class for classification purposes. It also confirms the selection of number of components and free parameters performed in the previous section.

To provide a comparison between the proposed method (GMM classifier) and other methodologies, three more methods are considered for plaque classification. The first one is a Rayleigh mixture classifier which can be easily derived following the formulation of Section V-A, we will refer to this method as the RMM classifier. This classifier does not exactly follow the same philosophy as was proposed in [30] because we are interested not only in the classification but also in providing probability maps for further post-processing, and this can be of help for physicians in plaque detection or diagnosis. The RMM classifier presented in [30] does not adapt the RMMs to each tissue class in the image under study and, thus, the reliability of the fitting is reduced. The second is the NMM classifier, obtained in the same way as the RMM classifier. A comparison between the GMM classifier versus the RMM and the NMM classifiers will confirm once more that GMM not only describes the speckle patterns better but also provides more discriminative power as a classifier.

The third method considered for comparison is the one of [38], in which a set of 35 textural features directly extracted from the envelope data are used. The multi-class classification is tackled by a combination of binary classifiers into the error-correcting output codes (ECOC) framework [48]. Each binary classification is obtained by means of adaptive boosting [49] where the weak classifiers are decisions stumps [30]. We refer to this classifier as the textural classifier.

Results of the classification are shown in Table VII. This table was calculated by considering the whole data set for classification. Specificity was calculated as $K = TN/(TN + FP)$; sensitivity as $S = TP/(TP + FN)$; and precision as $P = TP/(TP + FP)$. Note that in all classifiers, the performance of detecting lipidic plaque is poorer

than the others. To better see the differences between the methods, the confusion matrices are shown in Table VIII.

The good performance for calcified classification becomes clear for all the classifiers because all of them correctly classify 29 out of 30 calcified plaques. Regarding lumen, the best are the textural and GMM classifiers, with a correct classification of 48 and 49 out of 50, respectively.

In the case of fibrotic plaques, the best classifications are obtained with the NMM and GMM classifiers, with a noticeable difference with respect to the textural classifier and RMM classifier. This result evidences the discriminative power of the GMM and NMM classifiers between fibrotic and lipidic tissues and how the GMM and NMM properly describe the nature of the speckle in both cases.

A very interesting case appears with the RMM classifier with the fibrotic tissue. Note that this classifier shows a clear bias to the lipidic tissue. The reason is that the PDF of the lumen shows a heavy tailed distribution which is very difficult to model with Rayleigh distributions. Thus, more Rayleigh components are needed for modeling the tail and that components of the lipidic and fibrotic tissues contribute for that purpose. This results in 6 lumen plaques misclassified as fibrotic and 18 fibrotic plaques misclassified as lipidic.

Regarding lipidic plaques, poorer results are observed for all the classifiers. The best performances are obtained by the textural classifier. However, all classifiers present some difficulties in distinguishing between lipidic and fibrotic tissues. This is an expected result because plaques usually present a mixed nature.

The overall accuracy shows that the GMM classifier provides an increase of 5% with respect to the textural classifier and 3% with respect the NMM classifier.

TABLE VIII. CONFUSION MATRICES.

Actual	Predicted			
	Calcified	Lipidic	Fibrotic	Lumen
RMM classifier				
Calcified	29	0	1	0
Lipidic	2	7	3	2
Fibrotic	2	18	5	0
Lumen	0	0	6	44
NMM classifier				
Calcified	29	0	1	0
Lipidic	2	5	4	3
Fibrotic	2	4	18	1
Lumen	0	3	0	47
Textural classifier				
Calcified	29	0	1	0
Lipidic	1	8	4	1
Fibrotic	0	12	12	1
Lumen	0	1	1	48
GMM classifier				
Calcified	29	0	1	0
Lipidic	1	6	5	2
Fibrotic	2	4	19	0
Lumen	0	1	0	49

RMM = Rayleigh mixture model; NMM = Nakagami mixture model; GMM = gamma mixture model.

C. Statistical Significance

The statistical significance of these results is studied by means of the Friedman and Bonferroni–Dunn tests [50]. These tests were selected because no equal variance between results can be assumed and the Gaussian hypothesis is not guaranteed.

The fractional ranking of each separate classification test for each plaque is shown in Table IX. Fractional ranking consists of assigning distinct ordinal numbers to each classifier even if they are equal (where the assignment is arbitrarily done). Then, for those classifiers that are compared equally, the rank average is assigned to each one. Note that the best rank is obtained for the GMM classifier, followed by the textural classifier, the NMM, and finally the RMM classifier. This result holds with the overall accuracy results of Table VII.

The Friedman test states that the null-hypothesis is that the differences on the measured classification performance are due to randomness. To reject or not reject this hypothesis, the Friedman statistic value is calculated as

$$\chi_F^2 = \frac{12N}{k(k+1)} \left(\sum_j r_j^2 - \frac{k(k+1)^2}{4} \right), \quad (22)$$

where $k = 4$ is the number of classifiers and $N = 119$ is the number of samples. In our case the result is $\chi_F^2 = 64.26$. However, a more thorough statistic is obtained by means of the Iman–Davenport correction of the Friedman statistic:

$$F_F = \frac{(N-1)\chi_F^2}{N(k-1) - \chi_F^2}. \quad (23)$$

In this case, the value obtained is $F_F = 25.90$. The statistic F_F is distributed by a Fisher–Senecdor distribution with parameters $(k-1) = 3$ and $(k-1)(N-1) = 354$, so the critical value of $F_{3,\infty}$ for a confidence of 95% is 2.68. The statistic value obtained is much higher than this critical value, so the null hypothesis can be rejected and we can conclude that differences of the classifications are not due to randomness.

To see whether the GMM classifier statistically improves the results of the textural classifier, the Bonferroni–Dunn test is applied. This test states that the performance of two classifiers is significantly different if the corresponding average ranks are higher than the following critical difference:

$$CD = q_\alpha \sqrt{\frac{k(k+1)}{6N}}, \quad (24)$$

where critical values q_α are based on the Studentized range statistic [50]. In our case, $q_\alpha = 2.128$ for a confidence of 90% and $q_\alpha = 2.394$ for a confidence of 95%. Then, the critical difference is $CD_{90} = 0.36$ and $CD_{95} = 0.40$ for a confidence of 90% and 95%, respectively. This

distance is smaller than the differences between the GMM and the NMM, so we can conclude that the GMM is significantly better than the others with a confidence of 95%. The NMM and the textural classifiers are not significantly different from each other and all of them are significantly better than the RMM classifier.

D. Probability Maps

Two examples of the probability of belonging to each tissue class are analyzed. Both examples are depicted in Fig. 7. These examples show the way the plaques are represented in polar images. Note that the lipidic and fibrotic cases are difficult to identify because both represent similar speckle pattern. Calcified plaques present a shadow below them and their identification is easier.

The probabilities of belonging to each tissue class for the example of Fig. 7(a) are depicted in Fig. 8. Note that in Fig. 7(a), the probability of belonging to the calcified tissue is almost 1 in all the regions labeled as calcified. The upper region with high probability of belonging to calcified class is due to the artifacts of the catheter. These artifacts do not pose a problem because they can be easily detected or each image can be cropped according to the diameter of the catheter. Lumen tissue also has high probabilities through the whole segmented area, and thus it is almost always correctly classified. The most problematic tissues are the fibrotic and lipidic tissues. In these cases, the distributions of tissues are quite overlapped and, for these two tissues, the probabilities are comparable. These effects are shown in Table X, where the classification was performed with three components and three tissue classes: calcified, lipidic/fibrotic, and lumen.

The same observation is reinforced by considering the probability maps computed from the example depicted in Fig. 7(b). These are shown in Fig. 9.

VII. CONCLUSIONS

This work proposes a plaque characterization method for IVUS images based on the probabilistic behavior of speckle in each tissue class in different tissue types. A gamma distribution is assumed for the probabilistic description of the speckle because it has shown better performance than the Rayleigh and Nakagami distributions under the operations of downsampling and interpolation of the echo envelope. Because each plaque type may present different echogenic content, a GMM is adopted for modeling each class. It was shown that the proposed GMM outperforms the Rayleigh mixture approach of [30].

TABLE IX. MEAN RANK FOR THE ACCURACY OF THE CLASSIFIERS.

Classifier	RMM	NMM	Textural	GMM
Mean rank	3.2	2.3	2.6	1.9

RMM = Rayleigh mixture model; NMM = Nakagami mixture model; GMM = gamma mixture model.

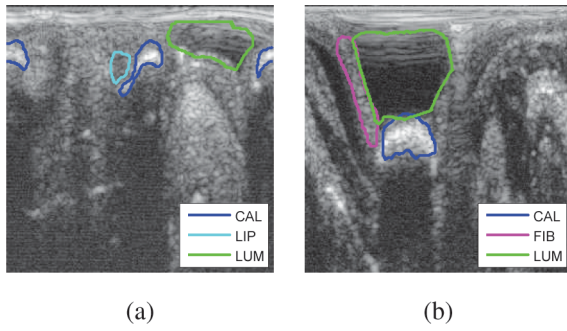


Fig. 7. Examples of presegmented IVUS images. Log compression was applied for a better visualization. Example image (a) shows two calcified plaques and a small lipidic plaque. Example (b) presents a fibrotic and a calcified plaque.

A classifier is proposed to obtain the posterior probability according to each tissue class. This classifier makes use of the GMM obtained for each test data which has been previously initialized with the GMM obtained during training. Four tissue classes were considered in this study: calcified, lipidic, fibrotic, and lumen. A leave-one-patient-out cross-validation technique was applied for validating the performance of the classifier, providing an overall accuracy of 86.56%. Statistical comparison with other methods showed that the proposed classifier is significantly better than the others. The overall gain of accuracy of the proposed method compared with the best of the others is about 5%.

The most problematic classes for classifying were lipidic and fibrotic tissues. This is due to the similarity between the two speckle patterns. A classification using three classes was also provided, considering fibrotic and

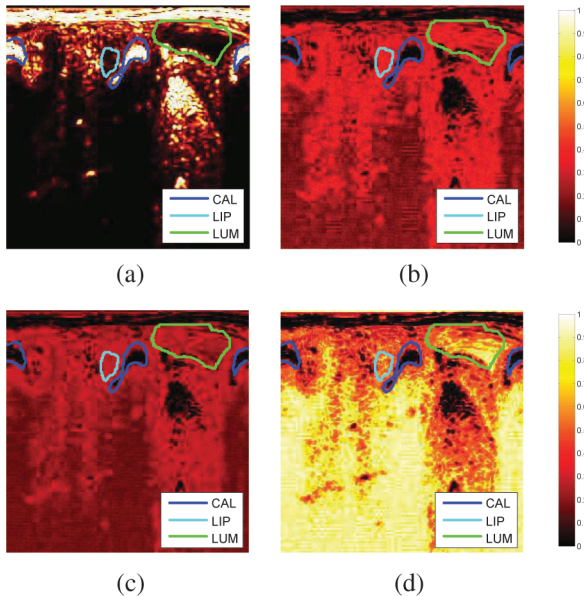


Fig. 8. Probability maps belonging to (a) calcified, (b) lipidic, (c) fibrotic, and (d) lumen tissue classes in the polar image of the example in Fig. 7(a).

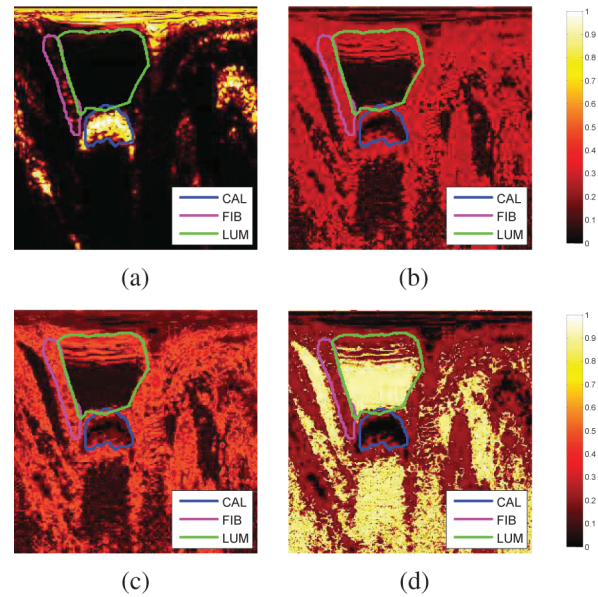


Fig. 9. Probability maps belonging to (a) calcified, (b) lipidic, (c) fibrotic, and (d) lumen tissue classes in the polar image of the example in Fig. 7(b).

lipidic as a joint class. In that case, an overall accuracy of 95.15% was obtained. This result shows that the proposed classifier offers a useful way to help physicians to detect and diagnose plaques.

Apart from the classification results, this classification scheme offers the possibility of representing probability maps of belonging to each tissue class. These probability maps can be codified into color maps to offer useful information for physicians. Additionally, probability maps can be useful for filtering and automatic segmentation purposes [51].

It is important to note that this work performs the validation with histologically validated plaque. It would be desirable to complete the study with the analysis of plaque in live subjects. However, because of the difficulties of having a gold standard in this case, the study with live subjects will be carried out as a future work.

Additionally, although the validation scheme was performed with a relatively low number of patients, which is always a limitation affecting the validation, the LOPO cross-validation technique gave rise to statistically significant results. Therefore, a larger data set would be desirable in future studies to increase even more the statistical significance by avoiding cross-validation techniques.

TABLE X. CLASSIFICATION PERFORMANCE FOR THREE COMPONENTS OF THE GMM INTO THREE CLASSES.

	Calcified	Lipidic/ Fibrotic	Lumen
Precision	92.59	93.94	97.67
Sensitivity	96.15	91.18	97.67

Total accuracy: 95.1456.

APPENDIX A

EXPECTATION MAXIMIZATION FOR MIXTURES OF GMM

The joint distribution of IID samples \mathbf{X} and the hidden RVs \mathbf{Z} and \mathbf{W} is given by

$$p(\mathbf{X}, \mathbf{Z}, \mathbf{W} | \Theta) = \prod_{i=1}^N p(x_i, z_i, w_{i,j} | \Theta), \quad (25)$$

where

$$\begin{aligned} p(x_i, z_i, w_{i,j} | \Theta) &= p(x_i | z_i, w_{i,j}, \Theta) p(w_{i,j} | z_i, \Theta) p(z_i | \Theta) \\ &= p(x_i | w_{i,j}, \Theta) p(w_{i,j} | z_i, \Theta) p(z_i | \Theta) \\ &= f_X(x_i | \Theta_{z_i, w_{i,j}}) \pi_{z_i, w_{i,j}} \nu_{z_i}. \end{aligned} \quad (26)$$

Note that the following equation holds:

$$\begin{aligned} p(x_i, \Theta) &= \sum_{z_i} \sum_{w_{i,j}} f_X(x_i | \Theta_{z_i, w_{i,j}}) \pi_{z_i, w_{i,j}} \nu_{z_i} \\ &= \sum_{j=1}^J \nu_j \sum_{r=1}^{R_j} \pi_{j,r} f_X(x_i | \Theta_{j,r}). \end{aligned} \quad (27)$$

Now, the log-likelihood function can be defined as

$$\begin{aligned} \mathcal{L}(\Theta | \mathbf{X}, \mathbf{Z}, \mathbf{W}) &= \sum_{i=1}^N \log p(x_i, z_i, w_{i,j} | \Theta) \\ &= \sum_{i=1}^N \log p(x_i | \Theta_{z_i, w_{i,j}}) + \sum_{i=1}^N \log p(w_{i,j} | \Theta) p(z_i | \Theta) \\ &= \sum_{i=1}^N \log f_X(x_i | \Theta_{z_i, w_{i,j}}) + \sum_{i=1}^N \log \pi_{z_i, w_{i,j}} + \sum_{i=1}^N \log \nu_{z_i}. \end{aligned} \quad (28)$$

The expectation of the log-likelihood function with respect to the hidden RVs when data \mathbf{x} and the previous estimate $\Theta^{(n)}$ are known is

$$\begin{aligned} \mathcal{Q}(\Theta | \Theta^{(n)}, \mathbf{X}) &= E_{\mathbf{Z}, \mathbf{W} | \Theta^{(n)}, \mathbf{X}} \{ \mathcal{L}(\Theta | \mathbf{X}, \mathbf{Z}, \mathbf{W}) \} \\ &= \sum_{i=1}^N \sum_{j=1}^J \sum_{r=1}^{R_j} \gamma_{i,j,r} (\log p(x_i | \alpha_{j,r}, \beta_{j,r}) + \log(\nu_j \pi_{j,r})), \end{aligned} \quad (29)$$

where $\gamma_{i,j,r} = p(Z_i = j, W_{i,j} = r | x_i, \Theta^{(n)})$, which can be easily calculated by means of the Bayes theorem:

$$\gamma_{i,j,r} = \frac{f_X(x_i | \Theta_{j,r}^{(n)}) \nu_j^{(n)} \pi_{j,r}^{(n)}}{\sum_{s=1}^J \sum_{r=1}^{R_j} f_X(x_i | \Theta_{s,r}^{(n)}) \nu_s^{(n)} \pi_{s,r}^{(n)}}. \quad (30)$$

The maximization process can be done in each of two terms separately. Then, the maximization step can be performed in the same way as was done in Section IV. Therefore, for the term with a dependence on the parameters ν_j and $\pi_{j,r}$ in (29), one can establish a Lagrange

function with Lagrange multipliers λ, μ_j for $j = \{1, \dots, J\}$. The constraints are those expressed in (13). The Lagrange function is

$$\begin{aligned} \Lambda(\nu, \pi, \lambda, \mu) &= \sum_{i=1}^N \sum_{j=1}^J \sum_{r=1}^{R_j} \gamma_{i,j,r} \log(\nu_j \pi_{j,r}) \\ &+ \lambda \left(\sum_{j=1}^J \nu_j - 1 \right) + \sum_{j=1}^J \mu_j \left(\sum_{r=1}^{R_j} \pi_{j,r} - 1 \right). \end{aligned} \quad (31)$$

Taking the derivative with respect to ν_j , for a fixed j , the following relation is deduced:

$$\nu_j \lambda = - \sum_i \sum_r \gamma_{i,j,r}, \quad (32)$$

therefore, summing over $j = \{1, \dots, J\}$, one obtains $\lambda = -N$. Thus, the value of ν_j that maximizes $\Lambda(\nu, \pi, \lambda, \mu)$ is

$$\nu_j^{(n+1)} = \frac{1}{N} \sum_{i=1}^N \sum_{r=1}^{R_j} \gamma_{i,j,r}. \quad (33)$$

The calculation of $\pi_{j,r}$ is performed in the same way; the result is

$$\pi_{j,r}^{(n+1)} = \frac{\sum_{i=1}^N \gamma_{i,j,r}}{\sum_{i=1}^N \sum_{s=1}^{R_j} \gamma_{i,j,s}}. \quad (34)$$

Now, regarding the term of (29) which depends on the parameters of the distribution $\alpha_{j,r}$ and $\beta_{j,r}$, the process of deriving these parameters is analogous to the GMM model explained in Section IV. The process is based on solving the following equations:

$$\begin{aligned} \hat{\beta}_{j,r} &= \frac{1}{\hat{\alpha}_{j,r}} \frac{\sum_i \gamma_{i,j,r} x_i}{\sum_i \gamma_{i,j,r}} \\ \log(\hat{\alpha}_{j,r}) - \psi(\hat{\alpha}_{j,r}) &= \log \left(\frac{\sum_i \gamma_{i,j,r} x_i}{\sum_i \gamma_{i,j,r}} \right) - \frac{\sum_i \gamma_{i,j,r} \log(x_i)}{\sum_i \gamma_{i,j,r}}. \end{aligned} \quad (35)$$

From the estimated value $\hat{\alpha}_{j,r}$ that maximizes the log-likelihood, the estimate of $\hat{\beta}_{j,r}$ can be calculated. See Appendix B for solving this equation.

APPENDIX B
SOLVING $\psi(x) - \log(x) = K$

In this appendix, we demonstrate that the function $g(x) = \psi(x) - \log(x)$ is a strictly increasing function when $x > 0$. For this purpose, we make use of the demonstration of the convexity of $f(x) = \log \Gamma(x) - x \log x$ for $x > 0$ (see [52]).

The property of convexity of $f(x)$ just guarantees that the first derivative of $f(x)$ is monotonically non-decreasing. Thus, a more detailed analysis should be done. To this end, we recall the well-known expansion of the second derivative of $\log \Gamma(x)$ (see [52]):

$$\frac{d^2}{dx^2} \log \Gamma(x) = \frac{1}{x^2} + \frac{1}{(x+1)^2} + \frac{1}{(x+2)^2} + \dots, \quad (36)$$

with $x \neq 0, -1, -2, \dots$

Making use of (36), the second derivative of $f(x)$ can be expressed as

$$f''(x) = \frac{d^2}{dx^2} \log \Gamma(x) - \frac{1}{x} = \sum_{k=0}^{\infty} \frac{1}{(x+k)^2} - \frac{1}{x}. \quad (37)$$

The second term can be introduced in the sum by means of expressing it as the following telescoping series

$$\frac{1}{x} = \sum_{k=0}^{\infty} \frac{1}{x+k} - \frac{1}{x+k+1}. \quad (38)$$

This yields the following result:

$$\begin{aligned} f''(x) &= \sum_{k=0}^{\infty} \frac{1}{(x+k)^2} - \frac{1}{x+k} + \frac{1}{x+k+1} \\ &= \sum_{k=0}^{\infty} \frac{1}{(k+x)^2(1+k+x)} > 0, \end{aligned}$$

for $x > 0$.

This result demonstrates the convexity of $f(x)$ and also that $f'(x) = \psi(x) - \log(x) - 1$ is a strictly monotonic increasing function and so is the function $g(x) = \psi(x) - \log(x)$.

We are interested in calculating the value \hat{x} that follows (35) that, without loss of generality, can be stated as

$$\log(x) - \psi(x) = K, \quad (39)$$

where K is the second term of (35). Note that this constant K is positive unless all elements x_i are identical (a case that does not occur in practice) because of the Jensen's inequality [53]:

$$\log \left(\frac{\sum_i^N \gamma_i x_i}{\sum_i^N \gamma_i} \right) \geq \frac{\sum_i^N \gamma_i \log(x_i)}{\sum_i^N \gamma_i} \quad (40)$$

for any $x_i > 0$ and $\gamma_i > 0$.

An interval where the function $x \rightarrow \log(x) - \psi(x) - K$ changes its sign can be derived simply by applying the following result (see [54]),

$$\frac{1}{2x} < \log(x) - \psi(x) < \frac{1}{x}. \quad (41)$$

Hence, the solution $\hat{x} \in (1/(2K), 1/K)$ and any root-finding method can be efficiently used.

ACKNOWLEDGMENTS

The authors sincerely thank F. Ciompi, O. Pujol, J. Mauri, and P. Radeva from the Computer Vision Center at the Universitat Autònoma de Barcelona (Spain) for providing the IVUS images used in this work, as well as the conversion algorithms to convert the raw US RF data from polar coordinates to Cartesian representation.

The authors also wish to thank the referees for many valuable suggestions.

REFERENCES

- [1] L. G. Spagnoli, A. Mauriello, G. Sangiorgi, S. Fratoni, E. Bonanno, R. S. Schwartz, D. G. Piepgras, R. Pistolese, A. Ippoliti, and D. R. Holmes Jr., "Extracranial thrombotically active carotid plaque as a risk factor for ischemic stroke," *JAMA*, vol. 292, no. 15, pp. 1845–1852, 2004.
- [2] E. Escolar, G. Weigold, A. Fuisz, and J. N. Weissman, "New imaging techniques for diagnosing coronary artery disease," *CMAJ*, vol. 174, no. 4, pp. 487–495, 2006.
- [3] J. E. Wilhjelm, M.-L. M. Gronholdt, B. Wiebe, S. K. Jespersen, L. K. Hansen, and H. Sillesen, "Quantitative analysis of ultrasound B-mode images of carotid atherosclerotic plaque: Correlation with visual classification and histological examination," *IEEE Trans. Med. Imaging*, vol. 17, no. 6, pp. 910–922, 1998.
- [4] N. M. El-Barghouty, G. Geroulakos, A. Nicolaidis, A. Androulakis, and V. Bahal, "Computer-assisted carotid plaque characterisation," *Eur. J. Vasc. Endovasc. Surg.*, vol. 9, no. 4, pp. 389–393, 1995.
- [5] N. M. El-Barghouty, T. Levine, S. Ladva, A. Flanagan, and A. Nicolaidis, "Histological verification of computerised carotid plaque characterisation," *Eur. J. Vasc. Endovasc. Surg.*, vol. 11, no. 4, pp. 414–416, 1996.
- [6] M. I. Matsagas, S. N. Vasdekis, A. G. Gugulakis, A. Lazaris, M. Foteinou, and M. N. Sechas, "Computer-assisted ultrasonographic analysis of carotid plaques in relation to cerebrovascular symptoms, cerebral infarction, and histology," *Ann. Vasc. Surg.*, vol. 14, no. 2, pp. 130–137, 2000.
- [7] D. Gonzalo Vegas-Sánchez-Ferrero, M. Martín-Martínez, S. Aja-Fernández, and C. Palencia, "On the influence of interpolation on probabilistic models for ultrasonic images," in *IEEE Int. Symp. Biomedical Imaging*, 2010, pp. 292–295.
- [8] J. Seabra, J. Sanches, F. Ciompi, and P. Radeva, "Ultrasonographic plaque characterization using a Rayleigh mixture model," in *IEEE Int. Symp. Biomedical Imaging*, 2010, pp. 1–4.
- [9] J. W. Goodman, "Some fundamental properties of laser speckle," in *Laser Speckle and Related Phenomena* (Topics in Applied Physics, vol. 9–75). Berlin, Germany: Springer, 1975, pp. 1145–1150.
- [10] K. Copsey and A. Webb, "Bayesian gamma mixture model approach to radar target recognition," *IEEE Trans. Aerosp. Electron. Syst.*, vol. 39, no. 4, pp. 1201–1217, 2003.
- [11] M. J. Thijssen, "Ultrasonic speckle formation, analysis and processing applied to tissue characterization," *Pattern Recognit. Lett.*, vol. 24, no. 4–5, pp. 659–675, 2003.
- [12] P. M. Shankar, J. M. Reid, H. Ortega, C. W. Piccoli, and B. B. Goldberg, "Use of non-Rayleigh statistics for the identification of tumors in ultrasonic B-scans of the breast," *IEEE Trans. Med. Imaging*, vol. 12, no. 4, pp. 687–692, 1993.
- [13] P. Mohana Shankar, "A general statistical model for ultrasonic backscattering from tissues," *IEEE Trans. Ultrason. Ferroelectr. Freq. Control*, vol. 47, no. 3, pp. 727–736, 2000.
- [14] F. Destremes and G. Cloutier, "A critical review and uniformized representation of statistical distributions modeling the ultrasound echo envelope," *Ultrasound Med. Biol.*, vol. 36, no. 7, pp. 1037–1051, 2010.

- [15] R. F. Wagner, M. F. Insana, and D. G. Brown, "Statistical properties of radio-frequency and envelope-detected signals with applications to medical ultrasound," *J. Opt. Soc. Am. A*, vol. 4, no. 5, pp. 910–922, 1987.
- [16] L. Rayleigh, "On the resultant of a large number of vibrations of the same pitch and of arbitrary phase," *Philos. Mag.*, vol. 10, pp. 73–78, 1880.
- [17] R. F. Wagner, S. W. Smith, J. M. Sandrik, and H. Lopez, "Statistics of speckle in ultrasound B-scans," *IEEE Trans. Sonics Ultrason.*, vol. 30, no. 3, pp. 156–163, 1983.
- [18] C. B. Burckhardt, "Speckle in ultrasound B-mode scans," *IEEE Trans. Sonics Ultrason.*, vol. 25, no. 1, pp. 1–6, 1978.
- [19] S. O. Rice, "Mathematical analysis of random noise," *Bell Syst. Tech. J.*, vol. 23, no. 3, pp. 282–332, 1944.
- [20] M. Nakagami, "Study of the resultant amplitude of many vibrations whose phases and amplitudes are at random," *J. Inst. Electron. Commun. Eng. Jpn.*, vol. 24, no. 202, pp. 17–26, 1940.
- [21] T. A. Tuthill, R. H. Sperry, and K. J. Parker, "Deviations from Rayleigh statistics in ultrasonic speckle," *Ultrason. Imaging*, vol. 10, no. 2, pp. 81–89, 1988.
- [22] E. Jakeman, "Speckle statistics with a small number of scatterers," *Opt. Eng.*, vol. 23, no. 4, pp. 453–461, 1984.
- [23] E. Jakeman, "On the statistics of K-distributed noise," *J. Phys. Math. Gen.*, vol. 13, no. 1, pp. 31–48, 1980.
- [24] V. Dutt and J. F. Greenleaf, "Ultrasound echo envelope analysis using a homodyned k distribution signal model," *Ultrason. Imaging*, vol. 16, no. 4, pp. 265–287, 1994.
- [25] E. Jakeman and R. J. A. Tough, "Generalized K distribution: A statistical model for weak scattering," *J. Opt. Soc. Am. A*, vol. 4, no. 9, pp. 1764–1772, 1987.
- [26] T. Eltoft, "Modeling the amplitude statistics of ultrasonic images," *IEEE Trans. Med. Imaging*, vol. 25, no. 2, pp. 229–240, 2006.
- [27] M. Nakagami, "The m-distribution—A general formula of intensity distribution of rapid fading," in *Statistical Methods in Radio Wave Propagation, Proceedings of a Symposium Held June 18–20, 1958*, W. C. Hoffmann, Ed., Elmsford, NY: Pergamon Press, 1960, pp. 3–36.
- [28] F. Destremes, J. Meunier, M. F. Giroux, G. Soulez, and G. Cloutier, "Segmentation of plaques in sequences of ultrasonic B-mode images of carotid arteries based on motion estimation and a Bayesian model," *IEEE Trans. Biomed. Eng.*, vol. 58, no. 8, pp. 2202–2211, 2011.
- [29] R. K. Saha and M. C. Kolios, "Effects of cell spatial organization and size distribution on ultrasound backscattering," *IEEE Trans. Ultrason. Ferroelectr. Freq. Control*, vol. 58, no. 10, pp. 2118–2131, 2011.
- [30] J. C. Seabra, F. Ciompi, O. Pujol, J. Mauri, P. Radeva, and J. Sanches, "Rayleigh mixture model for plaque characterization in intravascular ultrasound," *IEEE Trans. Biomed. Eng.*, vol. 58, no. 5, pp. 1314–1324, 2011.
- [31] A. P. Dempster, N. M. Laird, and D. B. Rubin, "Maximum likelihood from incomplete data via the EM algorithm," *J. R. Stat. Soc., B*, vol. 39, no. 1, pp. 1–38, 1977.
- [32] T. K. Moon, "The expectation-maximization algorithm," *IEEE Signal Process. Mag.*, vol. 13, no. 6, pp. 47–60, 1996.
- [33] Z. Tao, H. D. Tagare, and J. D. Beatty, "Evaluation of four probability distribution models for speckle in clinical cardiac ultrasound images," *IEEE Trans. Med. Imaging*, vol. 25, no. 11, pp. 1483–1491, 2006.
- [34] M. M. Nillesen, R. G. Lopata, I. H. Gerrits, L. Kapusta, J. M. Thijsen, and C. L. de Korte, "Modeling envelope statistics of blood and myocardium for segmentation of echocardiographic images," *Ultrasound Med. Biol.*, vol. 34, no. 4, pp. 674–680, 2008.
- [35] P. M. Shankar, F. Forsberg, and L. Lown, "Statistical modeling of atherosclerotic plaque in carotid B mode images—A feasibility study," *Ultrasound Med. Biol.*, vol. 29, no. 9, pp. 1305–1309, 2003.
- [36] S. Atapattu, C. Tellambura, and H. Jiang, "A mixture gamma distribution to model the SNR of wireless channels," *IEEE Trans. Wirel. Comm.*, vol. 10, no. 12, pp. 4193–4203, 2011.
- [37] A. Taki, H. Hetterich, A. Roodaki, S. K. Setarehdan, G. Unal, J. Rieber, N. Navab, and A. Konig, "A new approach for improving coronary plaque component analysis based on intravascular ultrasound images," *Ultrasound Med. Biol.*, vol. 36, no. 8, pp. 1245–1258, 2010.
- [38] F. Ciompi, O. Pujol, C. Gatta, O. Rodriguez-Leor, J. Mauri-Ferre, and P. Radeva, "Fusing in-vitro and in-vivo intravascular ultrasound data for plaque characterization," *Int. J. Cardiovasc. Imaging*, vol. 26, no. 7, pp. 763–779, 2010.
- [39] A. Nair, B. D. Kuban, E. M. Tuzcu, P. Schoenhagen, S. E. Nissen, and D. G. Vince, "Coronary plaque classification with intravascular ultrasound radiofrequency data analysis," *Circulation*, vol. 106, no. 17, pp. 2200–2206, 2002.
- [40] W. C. Roberts and A. A. Jones, "Quantitation of coronary arterial narrowing at necropsy in sudden coronary death: Analysis of 31 patients and comparison with 25 control subjects," *Am. J. Cardiol.*, vol. 44, no. 1, pp. 39–45, 1979.
- [41] W. Härdle, *Smoothing Techniques: With Implementation in S (Springer Series in Statistics)*. New York, NY: Springer, 1990.
- [42] F. Destremes, J. Meunier, M.-F. Giroux, G. Soulez, and G. Cloutier, "Segmentation in ultrasonic B-mode images of healthy carotid arteries using mixtures of Nakagami distributions and stochastic optimization," *IEEE Trans. Med. Imaging*, vol. 28, no. 2, pp. 215–229, 2009.
- [43] R. M. Dudley, *Uniform Central Limit Theorems*, 1st ed., Cambridge, UK: Cambridge University Press, 1999.
- [44] M. A. T. Figueiredo and A. K. Jain, "Unsupervised learning of finite mixture models," *IEEE Trans. Pattern Anal. Mach. Intell.*, vol. 24, no. 3, pp. 381–396, 2002.
- [45] A. R. Webb, "Gamma mixture models for target recognition," *Pattern Recognit.*, vol. 33, no. 12, pp. 2045–2054, 2000.
- [46] D. M. Titterton, A. F. Smith, and U. E. Makov, *Statistical Analysis of Finite Mixture Distributions*. (Wiley Series in Probability and Mathematical Statistics). New York, NY: Wiley, 1992.
- [47] G. Schwarz, "Estimating the dimension of a model," *Ann. Stat.*, vol. 6, no. 2, pp. 461–464, 1978.
- [48] T. G. Dietterich and G. Bakiri, "Solving multiclass learning problems via error-correcting output codes," *J. Artif. Intell. Res.*, vol. 2, pp. 263–286, 1995.
- [49] R. E. Schapire, "Using output codes to boost multiclass learning problems," in *Proc. 14th Int. Conf. Machine Learning*, 1997, pp. 313–321.
- [50] J. Demšar, "Statistical comparisons of classifiers over multiple data sets," *J. Mach. Learn. Res.*, vol. 7, pp. 1–30, Dec. 2006.
- [51] G. Vegas-Sánchez-Ferrero, S. Aja-Fernández, M. Martín-Fernández, A. F. Frangi, and C. Palencia, "Probabilistic-driven oriented speckle reducing anisotropic diffusion with application to cardiac ultrasonic images," in *Proc. 13th Int. Conf. Medical Image Computing and Computer-Assisted Intervention: Part I*, 2010, pp. 518–525.
- [52] M. Merkle, "Logarithmic convexity and inequalities for the gamma function," *J. Math. Anal. Appl.*, vol. 203, no. 2, pp. 369–380, 1996.
- [53] I. Franjić, S. Khalid, and J. Pecarić, "On the refinements of the Jensen-Steffensen inequality," *J. Inequal. Appl.*, vol. 2011, art. no. 12, Jun. 2011.
- [54] H. Alzer, "On some inequalities for the gamma and psi functions," *Math. Comput.*, vol. 66, no. 217, pp. 373–389, 1997.



Gonzalo Vegas received the M.S. and Ph.D. degrees in telecommunication engineering from the University of Valladolid, Valladolid, Spain, in 2006 and 2013, respectively. In 2006, he joined the Laboratory of Image Processing, University of Valladolid, as a Researcher. He was a Visiting Researcher with the Center for Computational Imaging and Simulation Technologies in Biomedicine, Barcelona, Spain; Instituto Superior Tecnico, Lisboa, Portugal; and the Athena Research Team, INRIA, Sophia-Antipolis, France. His research interests include statistical and mathematical methods for image and signal processing. Dr. Vegas Sánchez-Ferrero was the recipient of an FPI grant from the Spanish Government.



Jose Seabra received the M.Sc. and Ph.D. degrees in biomedical engineering from the Technical University of Lisbon, Lisbon, Portugal, in 2007 and 2011, respectively. His Ph.D. thesis proposed an ultrasound image processing methodology for computing anatomical, echogenic, and textural features with the ultimate goal of improving the identification, characterization, and classification of the carotid artery plaque lesion.

Since 2011, he has been working as an R&D engineer in the iMagX project (Université Catholique de Louvain and Ion Beam Applications, s.a., Louvain-la-Neuve, Belgium) where he collaborates in the development of an innovative computer platform and image processing algorithms to improve cancer treatment in proton therapy.



Oriol Rodríguez-Leor received the M.D. degree in 1997 from the Universidad Rovira i Virgili. He is an Interventional Cardiologist at Hospital Universitari Germans Trias i Pujol, Badalona, and an Assistant Professor at the Universitat Autònoma de Barcelona. He has broad clinical and interventional experience and he is an expert in intracoronary ultrasound with a large number of publications in this field.

His clinical research areas are acute coronary syndrome, acute myocardial infarction, intravascular ultrasound, and coronary stent design.



Angel Serrano received the M.D. degree in 1985 from the Autonomous University of Barcelona. Since 1981, he has worked in the department of Pathology of the General Hospital of Granollers, Barcelona. His clinical research areas are gastrointestinal and respiratory pathology. He is member of the Catalan Society of Pathology. He is an associate professor of anatomical pathology at the Universitat Internacional de Catalunya (UIC).



Santiago Aja-Fernández received the Ingeniero de Telecomunicación and Ph.D. degrees from the University of Valladolid, Spain, in 1999 and 2003, respectively. He is an Associate Professor with the ETSI Telecomunicación, University of Valladolid, where he is also with the Laboratory of Image Processing (LPI). His research interests include medical image analysis and processing.

Photograph and biography for **César Palencia** were not available at time of publication.



Marcos Martín Fernández received the Ingeniero de Telecomunicación and the Ph.D. degrees from the University of Valladolid, Valladolid, Spain, in 1995 and 2002, respectively. He is an Associate Professor at the ETSI Telecomunicación, University of Valladolid, where he is currently teaching and supervising several master's degree and Ph.D. students. From March 2004 to March 2005, he was a Visiting Assistant Professor of Radiology at the Laboratory of Mathematics in

Imaging (Surgical Planning Laboratory, Harvard Medical School, Boston, MA) thanks to a Fulbright fellowship grant. His research interests are statistical methods for signal and image segmentation and filtering in multidimensional signal processing. He also works in the application of mathematical methods to solve image processing problems. He is also researching in the fields of magnetic resonance imaging, ultrasonic imaging, and electrophysiological signal analysis and synthesis. He is associated with the Laboratory of Image Processing (LPI) at the University of Valladolid, where he is currently performing his research. He is a reviewer of several international scientific journals and a member of the scientific committee of the IEEE International Conference on Image Processing (ICIP); the International Conference on Medical Image Computing and Computer-Assisted Intervention (MICCAI); the European Signal Processing Conference (EUSIPCO); the IEEE International Symposium on Bioinformatics and BioEngineering (BIBE); the IEEE International Conference on Acoustics, Speech, and Signal Processing (ICASSP); and the IEEE International Symposium on Biomedical Imaging (ISBI). He also participates in fellowship evaluation for the National Competence Centre in Biomedical Imaging (NCCBI), Switzerland. He has 120 published papers in scientific journals and conferences. His Hirsch index is 10, with more than 250 received cites (SCOPUS).



J. Miguel Sanches received the E.E., M.Sc., and Ph.D. degrees from the Lisbon Institute of Technology [Instituto Superior Técnico (IST)], Technical University of Lisbon (UTL), Portugal, in 1991, 1996, and 2003, respectively, and the habilitation (agregação) in 2013 from the University of Lisbon (UL) in biomedical engineering. He teaches at the recently created Department of Bioengineering (DBE) at the IST.

He is a researcher at the Institute for Systems and Robotics (ISR), and his work has been focused on biomedical engineering (BME); namely, in biological and medical image processing and statistical signal processing of physiological and behavioral data. Morphological and textural characterization of tissues from ultrasound (US) images for the diagnosis of the atherosclerotic disease of the carotid and diffuse diseases of the liver are central issues, but he is also working with fluorescence images of microscopy for biological quantification purposes.

Dr. Sanches is also involved in the development of signal processing algorithms for polysomnography data and smartphone applications for long-term monitoring for diagnosis of sleep disorders. He has been a senior member of the IEEE Engineering in Medicine and Biology Society since 2011 and a Member of the Bio Imaging and Signal Processing Technical Committee (BISP-TC) of the IEEE Signal Processing Society. He is also president of the Portuguese Association of Pattern Recognition (APRP), an affiliate of the International Association of Pattern Recognition (IAPR).